Mon. Not. R. Astron. Soc. **389,** 1727–1738 (2008) doi:10.1111/j.1365-2966.2008.13611.x

The quasar proximity effect at redshift $\langle z \rangle \simeq 2.6$ with the From Lines to Overdensities approach⋆

V. D'Odorico,[1]† M. Bruscoli,[2,3] F. Saitta,[1,2,4] F. Fontanot,[5] M. Viel,[1,6] S. Cristiani[1,6] and P. Monaco[2]

[1]*INAF-OATS, Via Tiepolo 11, 34143 Trieste, Italy*
[2]*Dipartimento di Astronomia, Università degli Studi di Trieste, Via Tiepolo 11, 34143 Trieste, Italy*
[3]*INAF-IRA, L.go E. Fermi 5, I-50125 Firenze, Italy*
[4]*European Southern Observatory, Karl-Schwarzschild-Str. 2, D-85748 Garching bei München, Germany*
[5]*Max-Planck-Institute for Astronomy, Königstuhl 17, D-69117, Heidelberg, Germany*
[6]*INFN/National Institute for Nuclear Physics, Via Valerio 2, I-34127 Trieste, Italy*

Accepted 2008 June 17. Received 2008 June 17; in original form 2008 May 6

ABSTRACT

We revisit the proximity effect produced by quasars (QSOs) at redshifts 2.1–3.3 applying the From Lines to Overdensities (FLO) approach to a sample of ∼6300 Lyα lines fitted in 21 high resolution, high signal-to-noise spectra. This new technique allows to recover the hydrogen-density field from the H I column densities of the lines in the Lyα forest, on the basis of simple assumptions on the physical state of the gas. To minimize the systematic uncertainties that could affect the density recovering in the QSO vicinity, we carefully determined the redshifts of the QSOs in our sample and modelled in detail their spectra to compute the corresponding ionizing fluxes. The mean density field obtained from the observed spectra shows a significant overdensity in the region within 4 proper Mpc from the QSO position, confirming that QSOs are hosted in high-density peaks. The absolute value of $\rho/\langle\rho\rangle$ for the peak is uncertain by a factor of ∼3, depending on the assumed QSO spectral slope and the minimum H I column density detectable in the spectra. We do not confirm the presence of a significant overdensity extending to separations of ∼15 proper Mpc from the QSO, claimed in previous works at redshifts $\langle z \rangle \simeq$ 2.5 and 3.8. Our best guess for the ultraviolet background (UVB) ionization rate based on the intergalactic medium (IGM) mean density recovered by FLO is $\Gamma_{\rm UVB} \simeq 10^{-12}\,{\rm s}^{-1}$. However, values of $\Gamma_{\rm UVB} \simeq 3 \times 10^{-12}\,{\rm s}^{-1}$ could be viable if an inverted temperature–density relation with index $\alpha \simeq -0.5$ is adopted.

Key words: intergalactic medium – quasars: absorption lines – cosmology: observations – large-scale structure of Universe.

1 INTRODUCTION

The ultraviolet radiation emitted by quasars (QSOs) is considered the dominant source of ionization of the intergalactic medium (IGM) at redshifts 2–4. Most of the absorption lines seen blue-ward of the Lyα emission in QSO spectra (the so-called Lyα forest) are ascribed to fluctuations in the low to intermediate density IGM (see Meiksin 2007, for a recent review). As a consequence, Lyα lines can be used as probes of the properties and redshift evolution of the ultraviolet (UV) ionizing background.

Observations show that the number density of Lyα lines increases with redshift, but within single QSO spectra the number density of Lyα lines decreases as the redshift approaches the QSO emission redshift. This effect was first noticed by Carswell et al. (1982) and confirmed by later studies (Murdoch et al. 1986; Tytler 1987). Bajtlik, Duncan & Ostriker (1988) called this deficiency of Lyα absorptions near the background QSO 'proximity effect' and attributed it to the increased ionization of the Lyα clouds near the QSO due to its ionizing flux. They used the proximity effect in 19 low-resolution QSO spectra to estimate the intensity of the UV background (UVB) radiation at the Lyman limit,[1] $J_{\rm LL}$, for which they found the value $\log J_{\rm LL} \simeq -21.0 \pm 0.5\,{\rm erg\,cm^{-2}\,s^{-1}\,Hz^{-1}\,sr^{-1}}$ over the redshift range $1.7 < z < 3.8$. Several other authors carried out this analysis on other data sets (Lu, Wolfe & Turnshek 1991; Kulkarni & Fall 1993; Bechtold 1994; Williger et al. 1994; Cristiani et al. 1995; Giallongo et al. 1996). Lu et al. (1991) found

⋆Based on observations collected at the European Southern Observatory (ESO) Very Large Telescope (VLT), Cerro Paranal, Chile – Programs 166.A-0106(A) and during commissioning and science verification of UVES.

†E-mail: dodorico@oats.inaf.it

[1] The Lyman limit corresponds to the hydrogen-ionization energy $E_{\rm ion} = 13.6\,{\rm eV}$ or $\lambda_{\rm LL} = 912$ Å.

the same result of Bajtlik et al. (1988) in the same redshift interval but using 38 QSO spectra. Bechtold (1994), with 34 low-resolution QSO spectra covering the range $1.6 < z < 4.1$, found $\log J_{\rm LL} \simeq -20.5$. This value, 3 times larger than that of Bajtlik et al. (1988) and Lu et al. (1991), was not confirmed by Giallongo et al. (1996). They obtained $\log J_{\rm LL} \simeq -21.3^{+0.08}_{-0.09}$, using 10 higher resolution ($R \sim 25\,000$) QSO spectra in the same redshift interval as Bechtold (1994). More recently, Scott et al. (2000) considered a sample of 74 intermediate-resolution QSO spectra in the redshift interval $1.7 < z < 4.1$, from which they obtained a value $\log J_{\rm LL} \simeq -21.1^{+0.15}_{-0.27}$. These authors paid a particular attention to the correct estimate of the systemic redshift of the QSOs. Indeed, if a QSO redshift lower than the true one is used in the analysis, the ionizing effect of the QSO on the Lyα clouds, and thus the derived value of $J_{\rm LL}$, are overestimated.

In the standard analysis of the proximity effect, it is assumed that the matter distribution is not altered by the presence of the QSO. The only difference between the gas close to and far away from the QSO is the increased photo-ionization rate due to the QSO emission. A consequence of this hypothesis is that there should be a correlation between the strength of the proximity effect and the luminosity of the QSO. However, observational results are not conclusive on this subject (e.g. Lu et al. 1991; Bechtold 1994; Srianand & Khare 1996; but see also Liske & Williger 2001). It is in fact likely that QSOs occupy overdense regions. Hierarchical models of structure formation predict that supermassive black holes, that are thought to power QSOs, are in massive haloes (Granato et al. 2004; Fontanot et al. 2006; da Ângela et al. 2008) which are strongly biased to high-density regions.

The main aim of this work is to investigate the density distribution of matter close to QSOs from the proximity effect. To this purpose, we applied the From Lines to Overdensities (FLO) technique, developed in Saitta et al. (2007, Paper I), to a sample of 21 high resolution, high signal-to-noise ratio (S/N) QSO spectra. FLO converts the list of H I column densities of Lyα lines in a QSO spectrum into the underlying $n_{\rm H}$ hydrogen-density field. This method significantly reduces the drawbacks of the line-fitting approach, in particular, the dependence on the fitting tool, the subjectivity of the result, and the strong dependence of statistics on the number of weak lines, which is in general poorly known. We could also constrain the value of the UVB ionization rate, $\Gamma_{\rm UBV}$,[2] by matching the recovered density field in the Lyα forest region with the mean cosmic density.

Similar analyses were performed in previous works using a different approach, based on the determination of the cumulative probability distribution function (CPDF) of pixel optical depth. Rollinde et al. (2005) studied the density structure around QSOs using 12 high-resolution spectra that belong also to our sample. These authors marginally detected the presence of an overdensity at separations $3 \lesssim r \lesssim 15$ proper Mpc, assuming a hydrogen-ionization rate $\Gamma_{\rm UVB} = 10^{-12}\,{\rm s}^{-1}$ (corresponding to $\log J_{\rm LL} \simeq -21.4$). Guimarães et al. (2007), using the same technique, investigated the distribution of matter density close to 45 high-redshift ($z_{\rm em} \sim 3.8$) QSOs observed at medium spectral resolution. Their study reveals gaseous overdensities on scales as large as ∼15 Mpc, with higher overdensities for brighter QSOs.

The paper is organised as follows: in Section 2, we introduce the FLO technique and describe an improvement to the method. Section 3 reports the details of the observed data sample, the QSO emission redshift and luminosity determination, and the fitting analysis. In Section 4, the proximity effect of QSOs on the surrounding gaseous medium is pointed out and the overdensity close to QSOs is reconstructed with FLO. The characteristics of the cosmological simulations used to obtain the mock spectra and the comparison with observations are described in Section 6. Our conclusions and the prospect for the future are listed in Section 7.

Throughout this paper, we adopt a Λ cold dark matter (ΛCDM) cosmology with the following values for the cosmological parameters at $z = 0$: $\Omega_{\rm m} = 0.26$, $\Omega_\Lambda = 0.74$, $\Omega_{\rm b} = 0.0463$, $n_s = 0.95$, $\sigma_8 = 0.85$ and $H_0 = 72\,{\rm km\,s^{-1}\,Mpc^{-1}}$. These parameters are consistent with the best-fitting values obtained from the latest results on the cosmic microwave background (Komatsu et al. 2008) and from other flux statistics of the Lyα forest (e.g. Viel, Haehnelt & Lewis 2006).

2 THE FLO TECHNIQUE

FLO was introduced in Paper I. The physical hypotheses at the base of this procedure are briefly described in the following paragraphs.

Traditionally, the analysis of the Lyα forest was based on the identification and Voigt fit of the absorption lines in order to derive the central redshift, the column density and the Doppler parameter (measuring the velocity dispersion in the line). This approach has two main drawbacks: (i) the subjectivity of the decomposition into components: the same complex absorption can be resolved by different scientists (or software tools) in different ways, both in the number of components and in the values of the output parameters for a single component; (ii) the blanketing effect of weak lines: they can be hidden by the stronger lines, so that their exact number density is unknown and has to be inferred from statistical arguments. Unfortunately, since the weak lines are also the most numerous, the uncertainty in their exact number is transformed into a systematic error of the computed statistical quantities.

The FLO technique extends the line-fitting approach by identifying a new statistical estimator describing the physical properties of the underlying IGM, the hydrogen density $n_{\rm H}$, which is linked to the measured H I column density through the formula (Schaye 2001):

$$N({\rm H\,I}) \simeq 3.7 \times 10^{13}\,{\rm cm^{-2}}\,(1+\delta)^{1.5-0.26\alpha} T_{0,4}^{-0.26} \Gamma_{12}^{-1} \times \left(\frac{1+z}{4}\right)^{9/2} \left(\frac{\Omega_{\rm b} h^2}{0.024}\right)^{3/2} \left(\frac{f_{\rm g}}{0.178}\right)^{1/2}, \quad (1)$$

where, $\delta \equiv n_{\rm H}/\langle n_{\rm H}\rangle - 1$ is the density contrast, $T_{0,4} \equiv T_0/10^4$ K is the temperature at the mean density, $\Gamma_{12} \equiv \Gamma_{\rm UVB}/10^{-12}\,{\rm s^{-1}}$ is the H photo-ionization rate due to the UVB, $f_{\rm g} \approx \Omega_{\rm b}/\Omega_{\rm m}$ is the fraction of the mass in gas and α is the index of the temperature–density relation for the IGM which depends on the ionization history of the Universe. Equation 1 relies on three main hypotheses: (i) Lyα absorbers are close to local hydrostatic equilibrium, that is their characteristic size will be typically of the order of the Jeans length ($L_{\rm J}$), which can be approximated as[3] (Nusser & Haehnelt 2000; Zaroubi et al. 2006):

$$L_{\rm J} \simeq 1.498 \left(\frac{\Omega_{\rm m} h^2}{0.135}\right)^{-1/2} \left(\frac{T_{0,4}}{1.8}\right)^{1/2} \left(\frac{\alpha+1}{1.6}\right)^{1/2} \left(\frac{1+z}{3.5}\right)^{-1/2}, \quad (2)$$

in comoving Mpc, where $h \equiv H_0/100\,{\rm km\,s^{-1}\,Mpc^{-1}}$ and the other parameters were already defined, (ii) the gas is in photo-ionization

[2] $\Gamma_{\rm UVB} \equiv 4\pi \int_{\nu_{\rm LL}}^{\infty} \sigma_\nu (J_\nu/h\nu) {\rm d}\nu$, where σ_ν is the photo-ionization cross-section, $\nu_{\rm LL}$ is the frequency at the Lyman limit and $J_\nu = J_{\rm LL}(\nu/\nu_{\rm LL})^{-\gamma}$.

[3] Note that the formula in the original papers has the wrong sign for the exponent of $\alpha + 1$.

equilibrium and (iii) the 'effective equation of state' (Hui & Gnedin 1997),

$$T = T_0\,(\delta + 1)^{\alpha}, \tag{3}$$

holds for the optically-thin IGM gas.

In order to apply equation (1), we have, first of all, to go through the Voigt-fitting process of the Lyα forest absorptions in a QSO spectrum. Then, to transform the list of H I column densities of Lyα lines into the matter density field which generated them, we have to perform the following steps.

(1) Group adjacent Lyα lines into absorbers of size of 1 L_J with column density equal to the sum of column densities and redshift equal to the weighted average of redshifts, using column densities as weights. The absorbers are created with a Friend-of-Friend algorithm:

(i) the spatial separation between all the possible line pairs is computed and the minimum separation is compared with L_J, computed at the N(H I)-weighted redshift mean of the pair;

(ii) if the two lines of the pair are more distant than L_J, they are classified as two different absorbers, stored and deleted from the line list;

(iii) if the two lines are closer than L_J, they are replaced in the line list by one line with a redshift equals to the N(H I)-weighted mean of the two redshifts and a column density equals to the sum of the two-column densities;

(iv) the procedure is iterated until all the lines are converted into absorbers.

(2) Transform the list of column densities of absorbers into a list of δ inverting equation 1.

(3) Bin the redshift range covered by the Lyα forest into steps of 1 L_J and distribute the absorbers on to this grid, proportionally to the superposition between absorber size (which is again 1 L_J) and bin. Two cases are considered for the treatment of the empty bins: in the 'lower limit' case the bin is filled with an absorber of null-column density (corresponding to $\delta = -1$), while in the 'upper limit' case the bin is filled with an absorber with hydrogen density contrast corresponding to the minimum detectable column density in our data, $\log N(\mathrm{H\,I}) = 12\,\mathrm{cm}^{-2}$, at the redshift of the bin.

For the IGM parameters in equations (1) and (2), we adopted the same values of paper I: $T_{0,4} = 1.8$, $\Gamma_{12} = 1$ and $\alpha = 0.6$.

2.1 An improvement of the FLO method

In paper I, we tested the quality of the density reconstruction of FLO using synthetic QSO spectra drawn from a cosmological simulation (the same that is described in Section 6). Figs 1 and 2 show the results of those tests. Both the true density field and the reconstructed one along the simulated lines of sight (LOS) were rebinned into steps of one Jeans length. The recovered density field from the simulated LOS presents two main problems: (i) most of the points of the true density field belonging to underdense regions are not recovered with the correct δ-value, they are accounted for as empty bins or, for those approaching the average density, their value is overestimated and they are moved to moderately overdense regions; (ii) the number of points in the overdense regions are overestimated due to a systematic assignment of larger than true δ-values to those points. The latter effect causes also an overestimate of the average δ of the distribution which is 40–50 per cent higher than that of the true density field. In paper I, we solved this problem by normalizing both the true and the reconstructed δ field in order to have the same mean value, $\langle \delta + 1 \rangle = 1.0$. This solution is not viable for the present analysis,

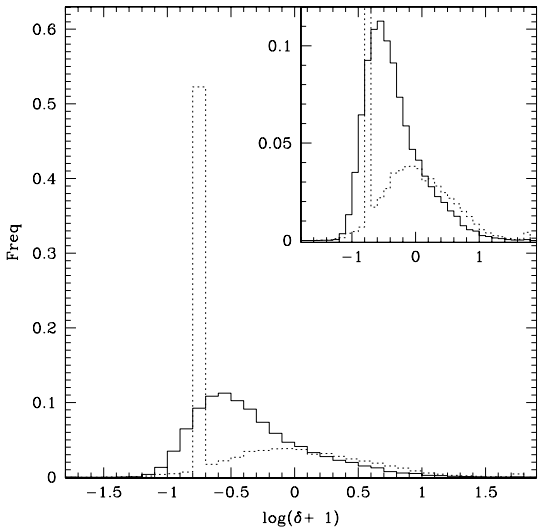

Figure 1. Distribution of the fraction of bins as a function of their $\log(\delta + 1)$-value for the true field (solid line) and the recovered one (dotted line) from the simulated LOS in the upper-limit case. The smoothing scale is the Jeans length.

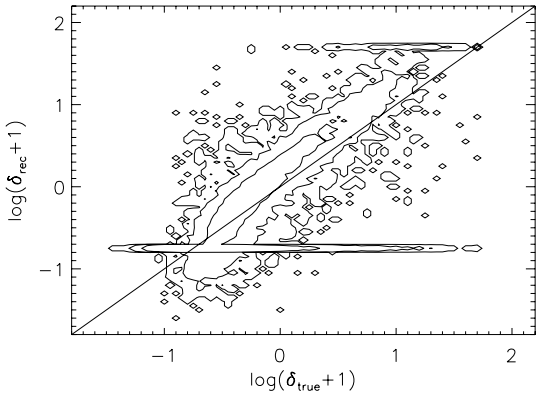

Figure 2. Contour scatter plot of the true versus reconstructed δ fields from simulations in the upper-limit case. The smoothing scale is the Jeans length. The contours show the number density of pixels which increases by a factor of 10 at each level.

so we looked for the physical reasons of the wrong reconstruction in order to improve the performances of FLO.

The failure in reproducing the underdense regions is likely due to the fact that gas below the average density is still expanding and our primary hypothesis, the local hydrostatic equilibrium, cannot be applied. There is no simple solution to this problem, however, we have already tested in paper I that underdense regions have a negligible effect on statistical quantities.

The problem regarding the moderately overdense regions depends on the scale adopted for the reconstruction of the absorbers, the Jeans length L_J, which appears to be too large. As a consequence, absorbers have on average too large column densities which translate into an overestimate of the δ values for the overdense regions. The need for a smoothing length smaller than L_J to better reproduce the density field traced by the Lyα forest, was discussed in detail by Gnedin & Hui (1998). They affirmed that the correct filtering scale depends on the re-ionization history of the Universe and is in general smaller than the Jeans scale after re-ionization, and larger prior to it. We used equation (A4) of Gnedin & Hui (1998) to compute

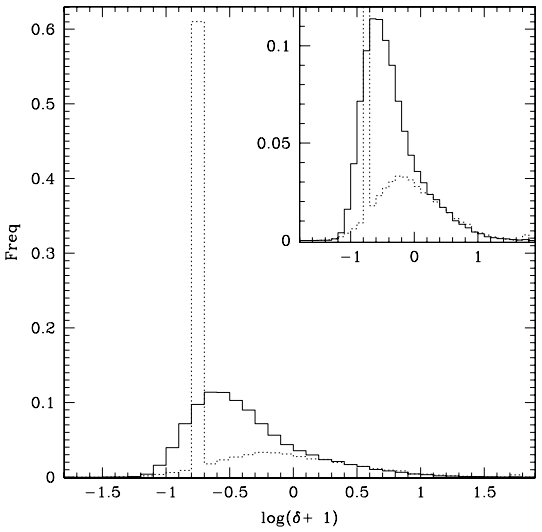

Figure 3. As in Fig. 1 but using a filtering scale $L_F \sim 0.7\ L_J$.

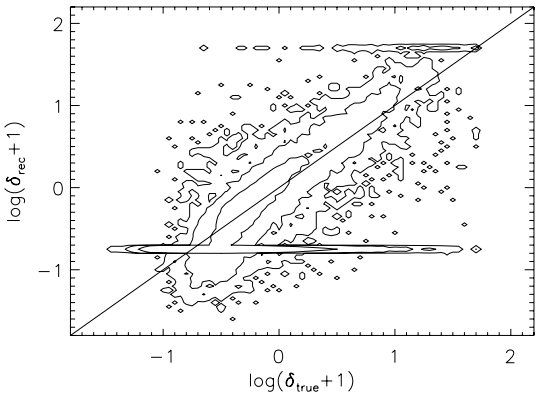

Figure 4. As in Fig. 2 but using a filtering scale $L_F \sim 0.7\ L_J$.

L_F, adopting $z_{rei} = 11$ and $z_{obs} = 2.5$. The results using the filtering scale $L_F \simeq 0.7\ L_J$ are shown in Figs 3 and 4. The moderately overdense regions are now successfully recovered both in the number of points and in the δ values, and the average δ of the distribution is in agreement with the true one within 10 per cent. We verified that varying the re-ionization redshift or the temperature at the mean density by ∼20 per cent does not have a significant effect on the density reconstruction process.

In the following analysis, the filtering scale L_F replaced the Jeans length in the FLO algorithm described before.

3 OBSERVED DATA SAMPLE

Most of the observational data used in this work were obtained with the UV–Visual Echelle Spectrograph (UVES; Dekker et al. 2000) at the Kueyen unit of the ESO VLT (Cerro Paranal, Chile) in the framework of the ESO Large Programme (LP): 'The Cosmic Evolution of the IGM' (Bergeron et al. 2004). Spectra of 18 QSOs were obtained in service mode with the aim of studying the physics of the IGM in the redshift range 1.7–3.5. The spectra have a resolution $R \sim 45\,000$ and a typical S/N of ∼35 and 70 per pixel at 3500 and 6000 Å, respectively. The wavelength range goes from 3000 to 10 000 Å, except for two intervals of about 100 Å, centred at ∼5800 and 8600 Å where the signal is absent, due to the gap between the two CCDs forming the red mosaic. In the spectra of the two QSOs at higher redshift (Q0420-388 and PKS216-158), there are three gaps centred at ∼5640 and 8600 Å of about 100 Å and at ∼6680 Å of width ∼50 Å. Details of the data reduction can be found in Chand et al. (2004) and Aracil et al. (2004). In particular, the continuum level was estimated with an automatic iterative procedure which underestimates the true continuum in the Lyα forest to about 2 per cent at $z \sim 2.3$. In the process of fitting the lines in the Lyα forest, we corrected the continuum level in the spectral intervals where it was clearly underestimated by interpolating the regions free from absorption with polynomials of 3rd order.

We added to the main sample three more QSO spectra with comparable resolution and S/N.

(i) J2233-606 (Cristiani & D'Odorico 2000). Data for this QSO were acquired during the commissioning of UVES in 1999 October.

(ii) HE1122-1648 (Kim et al. 2002). Data for this QSO were acquired during the science verification of UVES in 2000 February. The reduced and fitted spectrum was kindly provided to us by Tae-Sun Kim.

(iii) HS1946+7658 (Kirkman & Tytler 1997). Data for this QSO were acquired with Keck/HIRES in 1994 July.

In the following subsections, the procedure to derive the QSO emission redshift and luminosity and the Lyα line lists is described. Table 1 reports for each QSO in the sample the final emission redshift and how it was computed, the studied Lyα redshift range, the apparent magnitude of the QSO and the corresponding H ionization rate resulting from the three adopted QSO spectra, the luminosity at the Lyman limit and the radius of influence of the QSO ionizing flux. Fig. 5 shows the distribution in redshift of the Lyα forests for all the QSOs of the sample. We considered the range between 1000 km s^{-1} red-ward the Lyβ emission, to avoid contamination by Lyβ absorption lines, and the Lyα emission.

3.1 Estimate of the QSO systemic redshifts

The knowledge of the correct systemic redshift of the QSO is of fundamental importance when using the proximity effect to estimate both the intensity of the UV ionizing background and the density structure close to the QSO itself.

Emission redshifts of QSOs at $z_{em} \gtrsim 1.5$ are generally computed by the positions of the most prominent UV emission lines, in particular H I Lyα λ 1216 and C IV λ 1549. However, it was assessed by several studies (e.g. Gaskell 1982; Wilkes 1986; Espey et al. 1989; Corbin 1990; Boroson & Green 1992; Tytler & Fan 1992; Laor et al. 1995; Marziani et al. 1996; McIntosh et al. 1999; Vanden Berk et al. 2001; Sulentic et al. 2004) that high-ionization emission lines (e.g. C IV, N V λ 1240, C III] λ 1909 and H I Lyα) are on average blue-shifted by several hundreds of km s^{-1} with respect to low-ionization lines (e.g. O I λ1304, Mg II λ2798) and the permitted H I Balmer series. In contrast, redshifts from narrow forbidden lines (e.g. [O II] λ 3727, [O III] λ 5007) are observed to be within 100 km s^{-1} of the broad Mg II and Balmer lines. Furthermore, in local active galactic nuclei, redshifts from narrow forbidden lines showed agreement to ∼100 km s^{-1} of the accepted systemic frame determined by stellar absorption features and H I 21 cm emission in the host galaxies (Gaskell 1982; Vrtilek & Carleton 1985; Hutchings, Gower & Price 1987).

In order to estimate the correct redshift, we carried out a detailed analysis of the emission lines of the QSOs in our sample both using data from the literature and directly fitting the lines in the UVES spectra. In decreasing order of precision, we adopted the redshifts

Table 1. Relevant properties of the QSOs forming our sample. See text for further details.

QSO	z_{em}(Ref.)	line	$\Delta\, z_{Ly\alpha}$	b_J	r_F	$\Gamma/10^{40}$ F07	$\Gamma/10^{40}$ T02	$\Gamma/10^{40}$ HM	$\log L_{LL}$	r_{eq} (Mpc)
HE1341-1020[a]	2.142(1)	Mg II	1.6599-2.142	18.68	17.52	0.11 ± 0.03	0.10 ± 0.02	0.12 ± 0.02	30.712	2.9
Q0122-380	2.2004(2)	Hβ	1.709-2.2004	17.34	16.70	0.8 ± 0.3	0.5 ± 0.1	0.6 ± 0.1	31.267	5.5
PKS1448-232	2.224(1)	Mg II	1.729-2.224	17.09	16.87	1.0 ± 0.3	0.56 ± 0.09	0.6 ± 0.1	31.377	6.3
PKS0237-23	2.233(1)	Mg II	1.737-2.233	16.61	16.21	1.3 ± 0.6	0.8 ± 0.2	1.0 ± 0.2	31.573	7.9
J2233-606	2.248(1)	O I	1.7496-2.248	16.97	17.01	1.4 ± 0.2	0.66 ± 0.09	0.8 ± 0.1	31.437	6.7
HE0001-2340	2.265(1)	Mg II	1.764-2.265	16.74	16.46	1.2 ± 0.5	0.7 ± 0.2	0.9 ± 0.2	31.538	7.6
HE1122-1648[b]	2.40(3)		1.878-2.344	16.61	16.32	1.8 ± 0.5	1.0 ± 0.2	1.2 ± 0.2	31.679	8.9
Q0109-3518	2.4057(4)	[O III]	1.883-2.4057	16.72	16.37	1.8 ± 0.5	1.0 ± 0.2	1.1 ± 0.2	31.640	8.5
HE2217-2818[b]	2.412(1)		1.888-2.355	16.47	16.16	2.7 ± 0.5	1.3 ± 0.2	1.5 ± 0.2	31.744	9.6
Q0329-385	2.437(5)	Mg II	1.9096-2.437	17.20	16.91	1.6 ± 0.3	0.7 ± 0.1	0.8 ± 0.1	31.472	7.0
HE1158-1843[a,b]	2.448(1)		1.919-2.391	17.09	16.84	1.3 ± 0.2	0.70 ± 0.09	0.8 ± 0.1	31.525	7.4
HE1347-2457[a]	2.5986(4)	Hβ	2.046-2.5986	17.35	16.14	0.7 ± 0.3	0.7 ± 0.1	0.8 ± 0.1	31.542	7.6
Q0453-423	2.669(1)	O I	2.106-2.669	17.69	16.74	0.7 ± 0.4	0.5 ± 0.1	0.6 ± 0.1	31.451	6.8
PKS0329-255[b]	2.696(1)		2.129-2.635	17.88	17.71	0.8 ± 0.1	0.38 ± 0.06	0.44 ± 0.07	31.396	6.4
HE0151-4326[b]	2.763(1)		2.186-2.701	17.48	16.93	1.7 ± 0.4	0.9 ± 0.1	1.0 ± 0.1	31.594	8.1
Q0002-422	2.769(1)	O I	2.191-2.769	17.50	16.89	1.5 ± 0.4	0.8 ± 0.1	1.0 ± 0.1	31.589	8.0
HE2347-4342[a]	2.880(1)	O I	2.285-2.880	17.12	16.30	2.0 ± 0.7	1.3 ± 0.2	1.5 ± 0.2	31.810	10.4
HS1946+7658[a]	3.058(6)	O I	2.435-3.058	16.64	15.76	5 ± 1	2.7 ± 0.4	3.1 ± 0.5	32.118	14.8
HE0940-1050	3.0932(4)	Hβ	2.465-3.0932	17.08	16.08	3 ± 1	2.0 ± 0.3	2.3 ± 0.3	31.972	12.5
Q0420-388[a]	3.1257(1)	O I	2.493-3.1257	17.44	16.70	2.6 ± 0.5	1.2 ± 0.2	1.4 ± 0.2	31.848	10.8
PKS2126-158	3.292(7)	[O III]	2.633-3.292	17.54	16.37	4 ± 1	1.8 ± 0.3	2.0 ± 0.3	31.958	12.3

[a]QSOs with associated absorption systems.
[b]QSO not considered in the proximity study.
References: (1) this paper; (2) Sulentic et al. (2004); (3) Kim et al. (2002); (4) P. Marziani, private comm.; (5) Espey et al. (1989); (6) Fan & Tytler (1994) and (7) Scott et al. (2000).

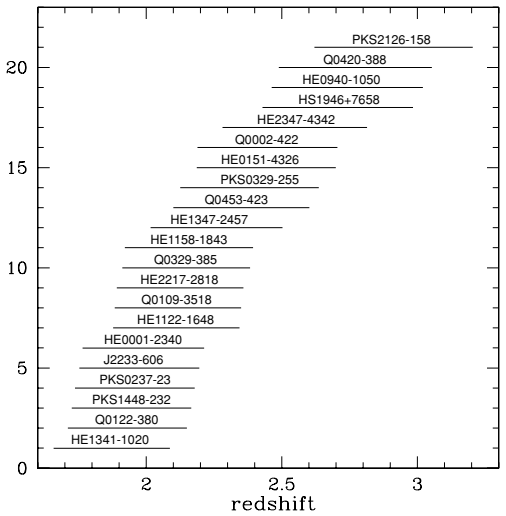

Figure 5. Lyα forest redshift coverage of the QSOs in our sample.

measured by: (i) narrow forbidden lines, mainly [O III], (ii) Hβ, (iii) Mg II and (iv) O I. There are five QSOs in the sample for which none of these lines was measured. We excluded those objects from the proximity study, disregarding the portion of the spectrum within 5000 km s^{-1} of the best estimate of the emission redshift (generally obtained from Lyα and/or C IV emission lines).

The determination of the redshifts from the UVES spectra were obtained by rebinning the region of the emission, normalizing it to the local continuum and fitting a Gaussian profile to the line. Table 1 gives the QSO redshifts and the details of the estimate.

3.2 Estimate of the QSO ionizing fluxes

Getting closer and closer to the QSO, the UV ionizing field becomes dominated by the intrinsic QSO emission flux. In order to derive the matter density distribution around the QSO using the observed variation of the absorption features in the QSO spectrum, a reliable determination of the intrinsic luminosity of the QSO has to be obtained.

Magnitudes of the objects in our sample were taken from the GSC-II catalogue (McLean et al. 2000) and are reported in Table 1. In order to estimate the corresponding intrinsic bolometric luminosity, we adopted the following procedure.

We considered the QSO template library defined in Fontanot et al. (2007), based on high-quality Sloan Digital Sky Survey (SDSS) QSO spectra in the redshift interval $2.2 < z < 2.25$. This redshift range was chosen in order to maximize the level of completeness of the sample and the wavelength interval long-wards of the Lyα emission. Moreover, in this redshift range the dynamical response of the SDSS spectrograph is such that the Lyα line is completely sampled in all spectra. In the original paper, the authors considered the rest-frame spectra of the 215 QSOs forming the final sample and they used a continuum fitting technique in order to extend the information blue-ward of the Lyα. A mean continuum slope $\gamma = 0.7 \pm 0.3$ was obtained for the objects in the library, where $f_\nu \propto \nu^{-\gamma}$ and f_ν (corresponding to $4\pi J_\nu$) are the QSO flux in units of erg cm^{-2} s^{-1} Hz^{-1}. Fontanot et al. (2007) demonstrated that this library is suitable for predicting QSO colours up to $z \simeq 5.2$.

We used the template spectra in the library to compute a synthetic b_J and r_F magnitude at each emission redshift listed in Table 1. For reproducing the b_J and r_F photographic magnitudes, the response of the spectral code PEGASE (Fioc & Rocca-Volmerange 1997) was assumed. Then, the templates were renormalized in each band separately, by requiring the synthetic magnitude to match the observed

one, and the renormalized spectra were used to give a prediction for the *AB* magnitudes at 912 Å ($M_{912}^{b_J}$ and $M_{912}^{r_F}$, respectively). The quantity $\Delta M_{912} = M_{912}^{b_J} - M_{912}^{r_F}$ was adopted as an estimator of the agreement between the slope of the template and the intrinsic slope of the considered QSO: we then associated to each observed QSO the template with the smaller ΔM_{912}. For 18 out of 21 QSOs in our sample, this procedure gave ΔM_{912} values lower than 0.001 mag. For the remaining three objects, the values were 0.1 (PKS0329-255), 0.2 (HE1347-2457) and 0.4 mag (HE1341-1020), respectively. In these cases, there was no template in the library which reproduced the correct intrinsic slope of the observed QSO. The ΔM_{912} can be taken as a measure of the systematic error on the luminosity computed for these three objects.

The selected and renormalized template spectra were completed in the region blue-ward of the Lyα emission using three possible extrapolations.

F07 the continuum slope of the template spectrum red-ward of the Lyα emission.

T02 a fixed power law with slope $\gamma = 1.8$ (Madau, Haardt & Rees 1999; Telfer et al. 2002).

HM a fixed power law with slope $\gamma = 1.5$ (Haardt & Madau 1996).

Then, the spectra were used to estimate the QSO monochromatic luminosities, L_ν (erg s^{-1} Hz^{-1}). The hydrogen photo-ionization rates due to the QSO radiation were obtained through the formula:

$$\Gamma_{\rm QSO}[{\rm s}^{-1}] = \frac{1}{4\pi r_{\rm abs}^2}\Gamma, \tag{4}$$

where $r_{\rm abs}$ is the distance (in cm) between the QSO emission redshift and the absorber, and Γ is obtained by integrating the monochromatic luminosity in the wavelength range $300 < \lambda < 912$ Å:

$$\Gamma = \int_{\nu_{\rm LL}} \frac{L_\nu}{h\nu}\,\sigma_\nu\,{\rm d}\nu, \tag{5}$$

where σ_ν is the absorbing cross-section for neutral hydrogen (Osterbrock 1989).

The error on Γ was computed by taking into account the uncertainties in the QSO magnitudes. We randomly extracted 100 values of $b_{\rm J}$ and $r_{\rm F}$ in the corresponding allowed range and we repeated the previous procedure. The obtained mean Γ values are in good agreement with the estimate based on the observed magnitudes, and we adopted the variance on the 100 realizations as the error on Γ. The values of Γ with their uncertainties, for the three investigated QSO continua, are reported in Table 1. The three estimates F07, T02 and HM agree within 2σ. In particular, the Γ for the T02 and HM models are always within 1σ. As a consequence, the differences between the results obtained adopting the three Γ values could be interpreted also as due to the uncertainties in the Γ itself.

The radius of the sphere of influence of each QSO in our sample is obtained by relating the intensity of the UV ionizing background at the Lyman limit, $J_{\rm LL}$, and the luminosity of the QSO at the same frequency, $L_{\rm LL}$, measured as described above,

$$r_{\rm eq} = \frac{1}{4\pi}(L_{\rm LL}/J_{\rm LL})^{1/2}. \tag{6}$$

The luminosities depend slightly on the adopted slope, however, the differences are small so we used the average of the three values to compute $r_{\rm eq}$. For the UVB, we adopted the value $J_{\rm LL} \sim 4 \times 10^{-22}$ erg cm^{-2} s^{-1} Hz^{-1} sr^{-1}, corresponding to an ionization rate $\Gamma_{\rm UVB} \simeq 10^{-12}$ s^{-1}. The resulting average $L_{\rm LL}$ and the radii expressed in proper Mpc are reported in Table 1.

3.3 Compilation of the line lists

All the lines in the Lyα regions of the LP QSOs plus J2233-606 were fitted with the FITLYMAN tool (Fontana & Ballester 1995) of the ESO MIDAS data reduction package.[4] In the case of complex saturated lines, we used the minimum number of components to reach $\chi^2 \leq 1.5$. Whenever possible, the other lines in the Lyman series were used to constrain the fit. The minimum H I column density detectable at 3σ with the S/N of the spectra of our sample is $\log N({\rm H\,I}) \simeq 12\,{\rm cm}^{-2}$.

Metals in the forest were identified and the corresponding spectral regions were masked to avoid effects of line blanketing. The same treatment was given to Lyα lines with column density $N({\rm H\,I}) \geq 10^{16}$ cm^{-2} since, on the one hand, strong H I lines can hide weaker lines as much as metal lines, and on the other hand the application of the FLO algorithm is valid only in the linear or mildly non-linear regime, or for overdensities $\delta \sim$ few $\times$ 10. We eliminated Lyα lines with Doppler parameters $b \leq 10\,{\rm km\,s}^{-1}$, that are likely unidentified metal absorptions. They represent about the 7 per cent of the total sample of Lyα lines. The output of this analysis is a list of Lyα lines for each QSO with central redshift, H I column density, Doppler parameter and the corresponding errors obtained with FITLYMAN.

The Lyα forests of the remaining two QSOs, HE1122-1648 and HS1946+7658, were fitted with the VPFIT[5] package. The same constraints on Doppler parameter and column density were applied to obtain the final Lyα line lists for these QSOs. The difference in the FLO results due to the different fitting software, FITLYMAN and VPFIT, is negligible and was discussed in Paper I.

4 THE PROXIMITY EFFECT

Moving closer to the QSO a decrease of the number density of Lyα absorption lines with respect to the mean value is expected.

We applied FLO to recover the density field in the neighbourhood of the QSOs in our sample,[6] deliberately neglecting the contribution of the QSO radiation field to the UV ionizing flux. The density field traced by the Lyα forest was computed in each QSO spectrum of our sample. The data were rebinned into bins of 8 proper Mpc in length. Bins covered by more than 33 per cent by masked intervals were eliminated from the final count for the single object. Then, in each bin, the mean of all the δ values contributing to that bin (one per QSO at maximum) was computed. The resulting δ-field is shown in Fig. 6 together with the number of QSOs contributing to each bin. The upper and lower-limit case are shown, the difference between the two reconstructions is negligible. The dashed line in the upper panel represents the average of δ values in the upper-limit case at separations larger than 20 Mpc, no longer affected by the ionizing flux from the QSO. The dotted lines are the 1 and 2σ standard deviations and the shaded region represents the 3σ level. A significant decrease of the density field is observed in the first bin at proper separation from the emitting QSO of less than 8 Mpc, corresponding to the average radius of influence of the QSOs in our sample.

[4] http://www.eso.org/midas

[5] http://www.ast.cam.ac.uk/~rfc/vpfit.html

[6] Note that due to the uncertainty in the emission redshifts, five QSOs were excluded from the computation of the proximity effect.

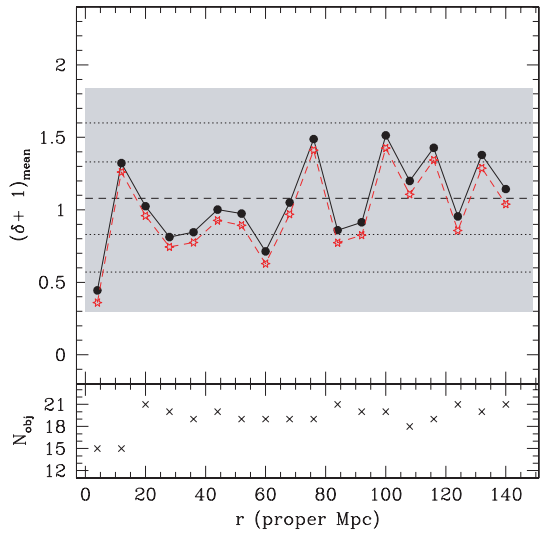

Figure 6. The mean of the δ field reconstructed around the QSOs in our sample, neglecting the effect of the UV flux from the QSO themselves. The solid dots represent the upper-limit case while the open stars trace the lower-limit case (see text). The shaded area marks the 3σ region for the upper limit case, the dotted lines mark the corresponding 1 and 2σ levels and the dashed line the average IGM density contrast. The lower panel shows the number of objects contributing to each bin.

4.1 The density structure around QSOs

In order to recover the density field in the region close to the emitting QSO, its ionizing flux has to be added to the UVB, and the total ionization rate has to be used in equation (1) of the FLO algorithm. We define Γ'_{12} as:

$$\Gamma'_{12} = \frac{\Gamma_{\rm UVB} + \Gamma_{\rm QSO}}{10^{-12}}, \quad (7)$$

where $\Gamma_{\rm QSO}$ was defined in equation (4). As explained in Section 3.2, the value of $\Gamma_{\rm QSO}$ depends on the adopted slope for the QSO continuum in the region blue-ward of the Lyman limit. We investigated how the three different assumptions for the slope influenced the final result.

In Fig. 7, we present the mean δ field for the lower- and the upper-limit case recovered from the spectra in our sample in the region within 20 Mpc from the radiating source in bins of 4 proper Mpc. We studied how the FLO output was modified by assuming different ionization rates for the UVB, $\Gamma_{12} = 1$–3, and different slopes for the QSO continuum.

The first important result of our analysis is that FLO recovers the overdensity hosting the QSOs in each one of the panels of Fig. 7. The second result is that the value of δ for the peak varies significantly depending on several factors that are discussed in the following.

(i) *Treatment of the empty bins*: at variance with the region away from the QSO, the lower- and upper-limit case in the treatment of the empty bins makes a difference of a factor of $\sim$2 for the δ value of the peak of the overdensity where the QSO resides. This is due to the QSO strong ionizing field that, when applied in equation (1), transforms even small column densities into large overdensities. Increasing the S/N of our spectra would decrease the minimum detectable H I column density, thus decreasing the difference between the two limiting cases.

(ii) *QSO continuum slopes*: the difference between the two extrapolations with the standard fixed power laws, with indexes $\gamma = 1.5$ and 1.8, is $\sim$10 per cent, while there is an increase in

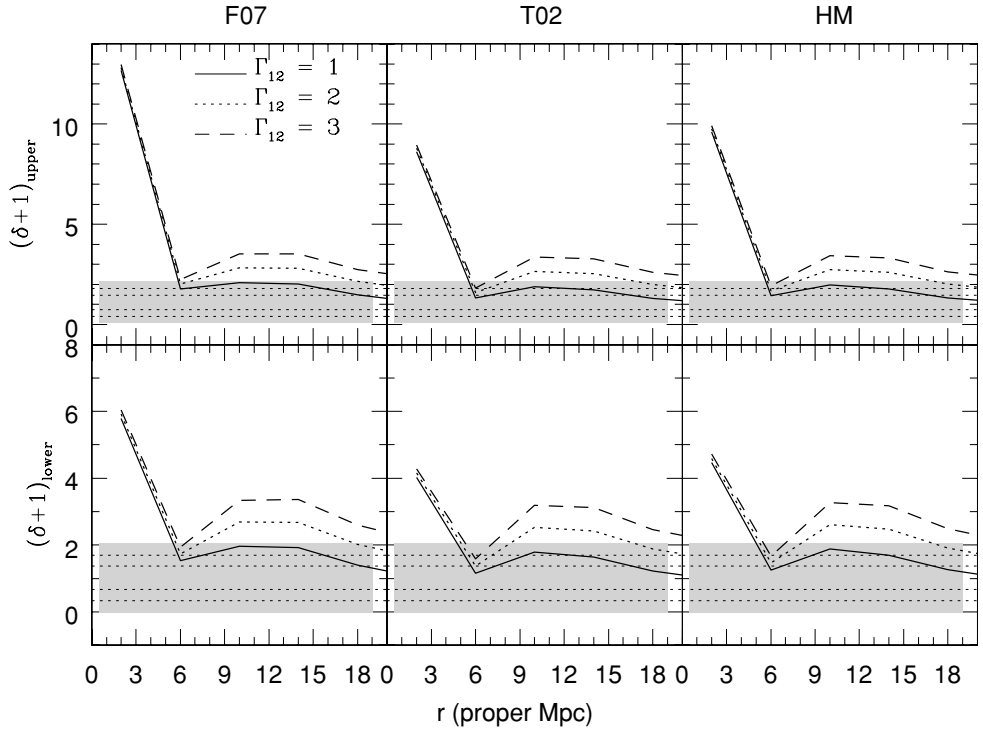

Figure 7. Mean δ field in the upper (top panels) and lower (bottom panels) limit case in the region close to the emitting QSO (which is located at $r = 0.0$) for the QSO spectra in our sample. In each row, the three panels differ for the adopted QSO continuum slope (see Section 3.2). The three curves in each panel differ for the adopted value of Γ_{12}. The 3σ fluctuations in the IGM region (far away from the QSO) are represented by the shaded area.

the peak value between ∼30 and 45 per cent when the F07 slopes are adopted. In the latter model, the continuum in the blue is obtained by extrapolating the slope red-ward of the Lyα emission, so it can be considered as a sort of upper-limit to the true continuum, that cannot be recovered due to contamination by the IGM absorption.

(iii) *Ionization rate of the UVB*: this parameter does not have any influence on the δ value for the QSO peak, as expected. On the other hand, the effect on the average value of the δ-field away from the QSO is significant and will be discussed in Section 4.3.

(iv) *QSO systemic redshifts*: the uncertainties in the emission redshifts of the QSOs whose spectrum was used to determine the overdensity are of the order of 100–200 km s^{-1} corresponding to ∼400–800 proper kpc at $z \simeq 2.5$. As a consequence, we do not expect a major influence on the value of the QSO overdensity which is computed in a bin of 4 proper Mpc. A significant improvement in the result would be obtained if the systemic redshift of all the QSOs in the sample would be measured with intermediate-resolution spectra in the infrared.

(v) *Associated absorption systems*: metal absorption systems within ∼5000 km s^{-1} (corresponding to ∼20 proper Mpc) from the emission redshift of the QSO are defined as *associated* to the QSO. Some of these systems could indeed be intrinsic to the QSO, that is they could be very close to the emitting region and their position could be determined only by the large velocity at which they were ejected from the QSO itself. Counting these lines as intervening would result in an overestimate of the density field in the proximity of the QSO. Six QSOs in our sample show associated absorption lines. Fig. 8 reports the comparison between the recovered density field of the total QSO sample and of the sample without associated absorption lines for the reference model and the F07 slopes. There is a decrease of ∼40 and 15 per cent in the δ value of the peak in the lower- and upper-limit case, respectively. A slight increase in the scatter of the IGM density field is also measured due to the lower statistics. The point at a separation of 98 Mpc is above the 3σ level, however, the fluctuation is due to a single QSO, PKS1448-232 and disappears when the QSO is eliminated from the sample.

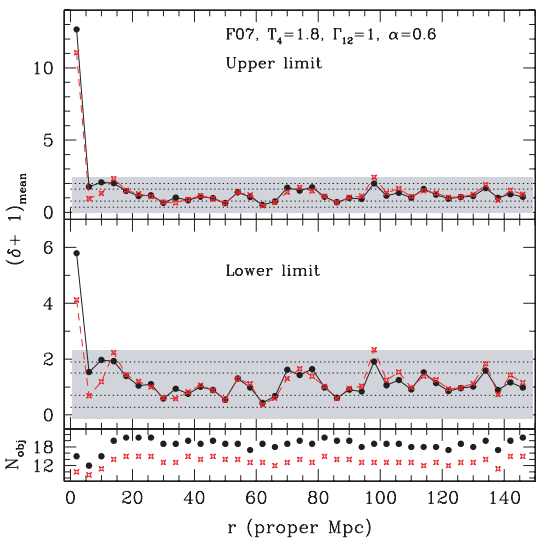

Figure 8. Comparison between the recovered average density field for the total sample (solid dots) and the sample without the QSOs with associated systems (empty stars) in the reference model with the F07 slopes. The shaded regions mark the 3σ interval and the dotted lines the 1 and 2σ level for the reduced sample. In the lower panel the number of objects for the two samples is reported.

4.2 Comparison with previous results

The density distribution in the region close to bright QSOs was studied in two previous works (Rollinde et al. 2005; Guimarães et al. 2007) with a different technique: the variation of the CPDF of the optical depth measured in the Lyα forest region away from and close to the QSO. The advantage of this method with respect to FLO is that the fitting of the lines is not necessary since the observed quantity used is the pixel-by-pixel transmitted flux. On the other hand, before investigating the change of the CPDF with the distance from the QSO, it is necessary to evaluate its evolution with redshift and subtract it. Then, the change in the CPDF has to be translated into a variation of the density field with a bootstrap technique (see Rollinde et al. 2005, for the detailed description).

Rollinde et al. (2005), using a subsample of our sample formed by 12 QSO spectra with $\langle z_{\rm em} \rangle \simeq 2.5$, found a significant overdensity for separations between ∼3 and 15 proper Mpc assuming $\Gamma_{12} < 3$. They assumed in the computation a QSO continuum with a fixed power law slope $\gamma = 0.5$ and a temperature–density relation index $\alpha = 0.5$. Guimarães et al. (2007) applied the same technique to a sample of 45 QSO spectra at intermediate resolution and at redshift $\langle z_{\rm em} \rangle \sim 3.8$. An overdensity extending to separations of ∼15 proper Mpc is detected adopting the parameters, $\Gamma_{12} = 1$, $T_{0.4} = 1$, $\alpha = 0.0$ and $\gamma = 0.7$. These authors claimed also the detection of a correlation between the overdensity and the luminosity: brighter QSOs reside in higher overdensities.

The main difference between our result and the previous ones is that we clearly detected an overdensity limited to a few Mpc from the QSO, while the results of the optical depth analysis showed a smooth decrease from the peak to the IGM density extending for more than 10 Mpc. In particular, the difference with the result at higher redshift by Guimarães et al. (2007) cannot be ascribed to a difference in QSO intrinsic luminosity, since the average luminosity of the two samples is the same: $\log L_{\rm LL} \simeq 31.7$. We will see in Section 5 that the cosmological hydro-simulations that we used for comparison show very narrow density peaks as found in our recovered density field. Very similar results were obtained by Faucher-Giguère et al. (2008) who investigated with hydrodynamical simulations the bias introduced by the QSO overdensity in the estimate of the UVB intensity from the proximity effect. They considered three ranges of masses $3.0 \pm 1.6 \times 10^{11}$, $3.0 \pm 1.6 \times 10^{11}$ and $6.0 \pm 3.2 \times 10^{12}\,{\rm M}_{\odot}\,h^{-1}$ for the dark matter haloes hosting QSOs in the simulations and averaging the results of 100 LOS obtained overdensity profiles extending to ∼3–5 proper Mpc at redshifts $z \simeq 2$–3.

4.3 Constraints on the IGM physical parameters

The FLO algorithm depends on the physical parameters of the IGM, in particular the temperature at the average density, the UVB ionization rate and the index of the temperature–density relation. We adopted for these parameters the values from the cosmological hydro-simulation used to validate the FLO performances in paper I. In turn, these values are in agreement with the most recent observational measurements (e.g. Ricotti, Gnedin & Shull 2000; Schaye et al. 2000; Scott et al. 2000; Tytler et al. 2004; Bolton et al. 2005).

In Fig. 7, we showed that values of the UVB ionization rate $\Gamma_{12} \geq 2$ (corresponding to UVB intensities at the Lyman limit, $\log J_{\rm LL} \geq -21.15$) are rejected at more than 3σ because they overestimate the average density of the IGM.

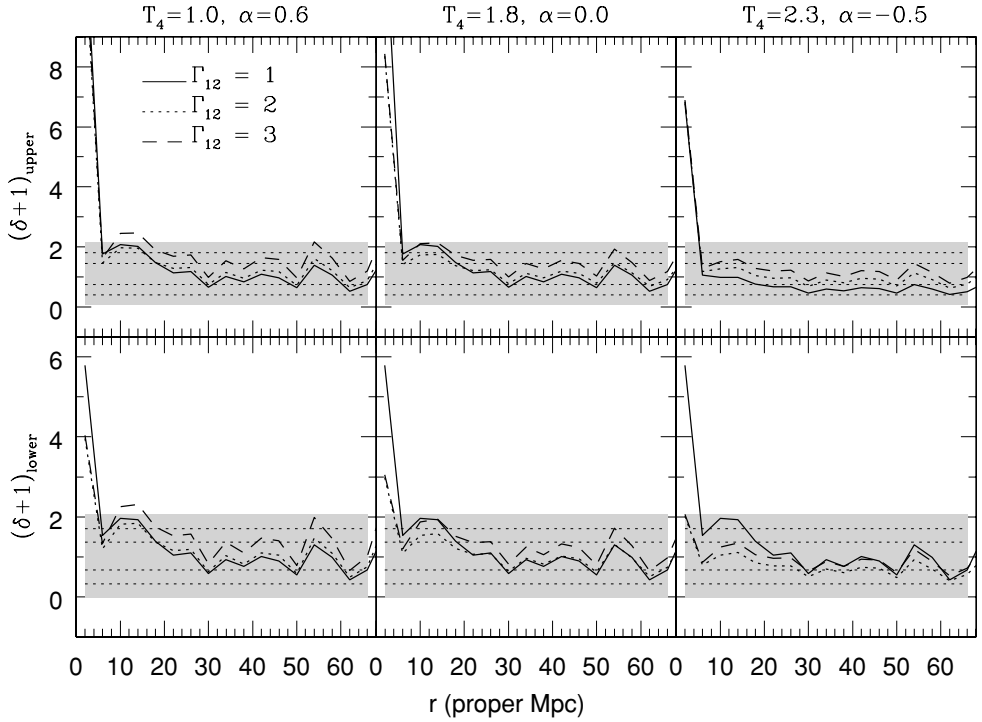

Figure 9. Variation of the FLO output δ-field with the physical parameters of the IGM. The solid line represents the fiducial model with $T_{0,4} = 1.8, \Gamma_{12} = 1$ and $\alpha = 0.6$ with the F07 QSO slopes. The dotted and dashed lines are obtained for $\Gamma_{12} = 2$ and $\Gamma_{12} = 3$, respectively, and varying the temperature and/or the index α as marked above the panels. The shaded regions and the dotted horizontal lines are the same of Fig. 7.

We investigated how the variation of the other two relevant parameters, $T_{0,4}$ and α, influence the reconstruction of the δ-field with FLO. The results are shown in Fig. 9. A temperature at the average density almost a factor of two lower than the reference one, which implied a decrease in the smoothing scale of ∼30 per cent, could reconcile values of $\Gamma_{12} = 2$ with the IGM average density but not values as large as $\Gamma_{12} = 3$. However, this temperature is at the lowest end of the measured temperatures in the IGM at the considered redshifts. Higher temperatures and high values of Γ_{12} allow to recover the correct IGM average density if a lower α index is adopted. In particular, an inverted temperature–density relation with $\alpha \sim -0.5$, as measured by Bolton et al. (2008) from the flux probability distribution function, would require a high temperature, and a high UVB ionization rate to recover the average IGM density.

However, the validity of the FLO reconstruction with a different set of parameters than the reference one needs to be verified with numerical simulations and we plan to do it in the next paper of the series.

5 COMPARISON WITH SIMULATIONS

We compared the reconstruction of the QSO overdensity by FLO with the average density field from a cosmological hydro-simulation in the proximity of the haloes that would likely harbour the QSOs in our sample.

5.1 Simulated LOS

The simulations were run with the parallel hydro-dynamical (TreeSPH) code GADGET-2 based on the conservative 'entropy-formulation' of SPH (Springel 2005). They consist of a cosmological volume with periodic-boundary conditions filled with an equal number of dark matter and gas particles. Radiative cooling and heating processes were followed for a primordial mix of hydrogen and helium. We assumed a mean UVB produced by QSOs and galaxies as given by Haardt & Madau (1996) with helium heating rates multiplied by a factor of 3.3 in order to better fit observational constraints on the temperature evolution of the IGM (Schaye et al. 2000). This background gives naturally a $\Gamma_{\rm UVB} \sim 10^{-12}$ at the redshifts of interest here (Bolton et al. 2005). The star-formation criterion is a very simple one that converts in collisionless stars all the gas particles whose temperature falls below 10^5 K and whose overdensity is larger than 1000. More details can be found in Viel, Haehnelt & Springel (2004). The cosmological model corresponds to a 'fiducial' ΛCDM Universe (the B2 series of Viel et al. 2004).

We used 2×400^3 dark matter and gas particles in a 120 h^{-1} comoving Mpc box. Having a large box size is crucial since the influence zone of the QSOs is usually of the order of some Mpc or tens of Mpc (see Table 1). The gravitational softening was set to $5\,h^{-1}$ kpc in comoving units for all particles. We analysed the output at $z = 2.2$ and run a Friend-of-Friend algorithm to identify the most massive collapsed haloes that should host the QSOs. We found about 400 (54) haloes whose total mass is larger than $2 \times 10^{12}\,{\rm M}_\odot\ h^{-1}$ ($10^{13}\,{\rm M}_\odot\ h^{-1}$). We then pierced the simulated box along the 400 LOS intersecting the centre of the haloes with $M \geq 2 \times 10^{12}\,{\rm M}_\odot\ h^{-1}$ and along random directions. This latter sample constitutes our 'control' sample. We explicitly checked that the correlation function of the haloes with masses larger than $2 \times 10^{12}\,{\rm M}_\odot\ h^{-1}$ is reasonably well fitted by a power-law function with $r_0 = 6\,{\rm Mpc}\ h^{-1}$ and slope -1.8 in agreement with observational results (Croom et al. 2005). Furthermore, it was recently found that QSOs could be typically hosted in haloes of mass $3 \times 10^{12}\,{\rm M}_\odot\ h^{-1}$ regardless of their luminosity and redshift (da Ângela et al. 2008).

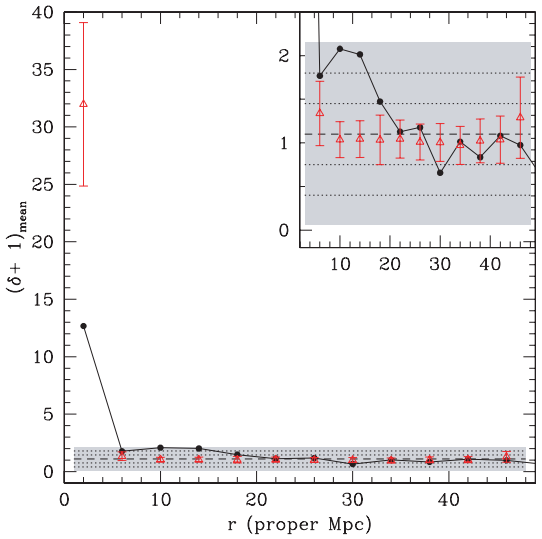

Figure 10. Comparison between the FLO average density field for the observed QSO sample (solid dots, upper limit case) in the reference model with the F07 slopes and the density field from simulations (empty triangles with 1σ error bars). The window in the upper-right corner is a zoom of the fluctuations at the mean level. The shaded area marks the 3σ regions, the dotted lines mark the 1 and 2σ and the dashed one the mean density level.

5.2 Comparison of the density fields

For each one of the 400 simulated LOS, the density contrast, the temperature and the peculiar velocity are known pixel by pixel. Peculiar velocities are small, typically less than 100 km s^{-1} and randomly oriented. However, since the observed density fields were recovered in redshift space, the mock LOS were modified by correcting the redshifts of the density field ($z_{\rm old}$) with the peculiar velocity field to obtain the density field in redshift space ($z_{\rm new}$) using the formula $v_{\rm pec}(z_{\rm old}) = c\,(z_{\rm new} - z_{\rm old})/[1 + (z_{\rm new} + z_{\rm old})/2]$ and the periodic-boundary conditions. Then, the mock LOS were shifted (applying the periodic-boundary condition) in order to have the peak of the most massive halo (where the QSO should reside) in the first pixel and the proper separation from this pixel was computed for all the other pixels. The total length of the simulated LOSs is ∼50 proper Mpc. The obtained density fields were finally rebinned into steps of 4 proper Mpc as in the case of the observed ones. The final simulated density field was computed by averaging in each bin the mean δ of 100 samples of 19 LOSs (the average number of objects per bin in the observed sample) extracted from the total sample of 400 mock LOSs with a bootstrap technique. The error bars on the final density field were computed from the standard deviation of the 100 samples.

The comparison between the simulated density field and the one recovered from observed spectra is plotted in Fig. 10. The simulated δ field is consistent with the mean IGM density down to 4 Mpc and up to 48 Mpc (see zoomed window). The disagreement between the simulated and observed density contrast in the first bin and, in particular, the large value of δ obtained from the mock spectra, could be explained by the fact that the considered simulations do not include in the most massive haloes the presence of the active galactic nuclei that would accrete part of the gas in the peak.

6 CONCLUSIONS

In this work, we used a sample of ∼6300 Ly α absorption lines obtained from high resolution, high-S/N spectra of 21 QSOs in the redshift range $2.1 \lesssim z_{\rm em} \lesssim 3.3$ and the FLO algorithm for the reconstruction of baryon density fields (described in details in Paper I) to investigate the baryon distribution as a function of the distance from the QSO.

The effect of the QSO radiation (supposed to be isotropic) dominates over the UVB in a sphere with radius varying from ∼3 to 15 Mpc for our sample, with an average of ∼8 Mpc. The increased ionization flux modifies the local line number density causing the so-called *proximity effect*, that was used in the past to estimate the intensity of the UVB at the Lyman limit. However, the local line number density is determined not only by the ratio between the UV flux from the QSO and the UVB but also by a variation of the density field due to the fact that QSOs likely lie on density peaks.

The recovery is extremely sensitive to the emission redshift and to the UV flux of the QSOs. We spent a significant effort to obtain, both from the literature and from the spectra at our disposal, the best estimates for the systemic redshifts of the QSOs in our sample in order to reduce the uncertainties to less than 100–200 km s^{-1}. For the 16 QSOs, for which the redshift was determined with $H\beta$, [O III] (5 QSOs) or with the O I, Mg II UV emission lines, the average velocity difference with respect to the determinations present in the literature (e.g. Kim et al. 2004, based mainly on the high-ionization UV lines and Lyα) is ~ -500 km s^{-1}. For the QSO UV flux, we adopted three different models: two with a power law with a fixed slope and one for which each QSO has its own slope obtained from the comparison with a spectral library. The resulting ionization rates for the three models are within a factor of 2.

We improved the performances of FLO with respect of paper I by adopting a smoothing scale ∼30 per cent smaller than the Jeans length, following the prescription by Gnedin & Hui (1998). This contrivance allows us to solve the problem of overestimation of the overdensities we had in paper I and to correctly recover the mean density in the IGM.

We applied the FLO algorithm to each QSO spectrum and recovered the sample-averaged δ field as a function of the distance from the emitting sources, in bins of 4 proper Mpc. The obtained results are described in the following sections.

6.1 QSO overdensity from the proximity effect

(i) If only the UVB ionization rate is adopted in equation (1) of FLO, neglecting the QSO radiation, a decrease of the mean density field significant at $\sim 2\sigma$ is observed within 8 proper Mpc of the emitting QSO, confirming the presence of a proximity effect.

(ii) When also the QSO ionization rate is taken into account an overdensity significant at more than 3σ is recovered at proper separations of less than 4 Mpc (first bin).

(iii) The absolute δ-value of the QSO overdensity is uncertain by an overall factor of ∼3. A factor of ∼2 variation is due to the lower- and upper-limit δ value derived for the empty bins during the field reconstructions: corresponding to no absorber or to one absorber with the minimum H I column density detectable in our sample, respectively. This uncertainty can be improved by using more spectra with a larger S/N. Another factor of ∼1.1–1.5 is due to the different assumptions for the QSO continuum in the region blue-ward of the Lyα emission.

(iv) The uncertainty on the systemic redshift of the QSOs used to determine the density distribution in their neighbourhood is $\lesssim$200 km s^{-1} corresponding to separations $\lesssim$800 proper kpc. As a consequence, it should have negligible effects on the δ value of the peak.

(v) We compared the resulting density field with the average density field in the proximity of massive haloes ($M > 2 \times 10^{12}\,\mathrm{M}_{\odot}\,h^{-1}$) in a cosmological hydro-simulations. The two distributions are in reasonably good agreement.

(vi) There is a significant discrepancy between our results and the previous determinations of the matter distribution around QSOs, obtained with the optical depth statistics (ODS, Rollinde et al. 2005; Guimarães et al. 2007) at redshifts $\langle z_{\rm em}\rangle \simeq 2.5$ and 3.8. The ODS method recovers gaseous overdensities extending to scales as large as ∼15 Mpc while our overdensity is limited to a region closer than 4 proper Mpc from the QSO. We would need to increase our sample, in particular with QSOs without associated systems in order to study if the brightest objects resides in more extended density peaks.

6.2 Constraints on the IGM physical parameters

(i) In the hypothesis of a temperature of the gas at the mean density $T_0 = 1.8 \times 10^4$ K and an index of the temperature–density relation for the IGM $\alpha = 0.6$, an UVB ionization rate of $\Gamma_{\rm UVB} \simeq 10^{-12}\,\mathrm{s}^{-1}$ gives the correct IGM mean density. On the other hand, $\Gamma_{\rm UVB} \simeq 2 \times 10^{-12}$ and $3 \times 10^{-12}\,\mathrm{s}^{-1}$ are excluded at more than 2 and 3σ, respectively, because the recovered FLO IGM density field overestimates the mean density.

(ii) Values of $\Gamma_{\rm UVB} > 10^{-12}\,\mathrm{s}^{-1}$ can be reconciled with the correct IGM mean density if different combination of T_0 and α are adopted. In particular, an inverted temperature–density relation with $\alpha \simeq -0.5$ used in the FLO algorithm gives the correct IGM mean density for $\Gamma_{\rm UVB} \simeq 3 \times 10^{-12}\,\mathrm{s}^{-1}$ and $T_0 \simeq 2.3 \times 10^4$ K. Such large values of the ionization rate could arise as a consequence of the He II reionization at $z \sim 3$ and of UVB fluctuations (e.g. Meiksin & White 2004). The performances of FLO with different set of parameters than the reference one have, however, to be tested with numerical simulation. We defer the details of this analysis to a future paper.

6.3 Limiting factors and future developments

(i) Most of the high-redshift QSOs have redshifts determined from UV-emission lines which are known to be systematically shifted with respect to systemic redshifts. This is particularly critical for proximity effect studies both along and transverse to the LOS. An improvement in this sense is expected from the new intermediate resolution, UV to near-IR spectrograph X-Shooter at the VLT (Vernet et al. 2008), that will be operative from the first trimester of 2009.

(ii) The temperature of the IGM gas at the mean density is highly uncertain. Its best determinations date back to 2000, the evidence of a jump in its value at $z \sim 3$ was marginal and should be verified with the present larger samples of high-resolution, high-S/N QSO spectra. Furthermore, those temperature estimates are used in many cosmological hydro-simulations to renormalize the ionizing background intensity.

(iii) The intensity and nature of the UV background is another unsolved riddle which should require a new observationally-based determination (with the caveat in i) since the present simulations are only now starting to have the resolution and the physics (e.g. the radiative transfer) needed to derive it self-consistently.

ACKNOWLEDGMENTS

We are grateful to A. Grazian for useful discussions and to an anonymous referee for his/her constructive comments. It is a pleasure to thank P. Marziani and collaborators for having shared the information on the systemic redshift of 3 QSOs of our sample before publication. Numerical computations were done on the COSMOS supercomputer at DAMTP and at High Performance Computer Cluster (HPCF) in Cambridge (UK). COSMOS is a UK-CCC facility which is supported by HEFCE, PPARC and Silicon Graphics/Cray Research.

REFERENCES

Aracil B., Petitjean P., Pichon C., Bergeron J., 2004, A&A, 419, 811
Bajtlik S., Duncan R. C., Ostriker J. P., 1988, ApJ, 327, 570
Bechtold J., 1994, ApJS, 91, 1
Bergeron J. et al., 2004, The Messenger, 118, 40
Bolton J. S., Haehnelt M. G., Viel M., Springel V., 2005, MNRAS, 357, 1178
Bolton J. S., Viel M., Kim T.-S., Haehnelt M. G., Carsweel R. F., 2008, MNRAS, 386, 1131
Boroson T. A., Green R. F., 1992, ApJS, 80, 109
Bryan G. L., Machacek M. E., 2000, ApJ, 534, 57
Carswell R. F., Whelan J. A. J., Smith M. G., Boksenberg A., Tytler D., 1982, MNRAS, 198, 91
Chand H., Srianand R., Petitjean P., Aracil B., 2004, A&A, 417, 853
Corbin M. R., 1990, ApJ, 357, 346
Cristiani S., D'Odorico V., 2000, AJ, 120, 1648
Cristiani S., D'Odorico S., Fontana A., Giallongo E., Savaglio S., 1995, MNRAS, 783, 1016
Croom S. M. et al., 2005, MNRAS, 356, 415
da Ângela J. et al., 2008, MNRAS, 383, 565
Dekker H., D'Odorico S., Kaufer A., Delabre B., Kotzlowski H., 2000, SPIE, 4008, 534
Espey B. R., Carswell R. F., Bailey J. A., Smith M. G., Ward M. J., 1989, ApJ, 342, 666
Fan X.-M., Tytler D., 1994, ApJS, 94, 17
Faucher-Giguère C.-A., Lidz A., Zaldarriaga M., Hernquist L., 2008, ApJ, 673, 39
Fioc M., Rocca-Volmerange B., 1997, A&A, 326, 950
Fontana A., Ballester P., 1995, The Messenger, 80, 37
Fontanot F., Monaco P., Cristiani S., Tozzi P., 2006, MNRAS, 373, 1173
Fontanot F., Cristiani S., Monaco P., Nonino M., Vanzella E., Brandt W. N., Grazian A., Mao J., 2007, A&A, 461, 39
Gaskell C. M., 1982, ApJ, 263, 79
Giallongo E., Cristiani S., D'Odorico S., Fontana A., Savaglio S., 1996, ApJ, 466, 46
Gnedin N. Y., Hui L., 1998, MNRAS, 296, 44
Granato G. L., De Zotti G., Silva L., Bressan A., Danese L., 2004, ApJ, 600, 580
Guimarães R., Petitjean P., Rollinde E., de Carvalho R. R., Djorgovski S. G., Srianand R., Aghaee A., Castro S., 2007, MNRAS, 377, 657
Haardt F., Madau P., 1996, ApJ, 461, 20
Hui L., Gnedin N. Y., 1997, MNRAS, 292, 27
Hutchings J. B., Gower A. C., Price R., 1987, AJ, 93, 6
Kim T.-S., Carswell R. F., Cristiani S., D'Odorico S., Giallongo E., 2002, MNRAS, 335, 555
Kim T.-S., Viel M., Haehnelt M. G., Carswell R. F., Cristiani S., 2004, MNRAS, 347, 355
Kim T.-S., Bolton J. S., Viel M., Haehnelt M. G., Carsweel R. F., 2007, MNRAS, 382, 1657
Kirkman D., Tytler D., 1997, ApJ, 484, 672
Komatsu E. et al., 2008, ApJS, submitted (arXiv:0803.0547)
Kulkarni V. P., Fall S. M., 1993, ApJ, 413, L63
Laor A., Bahcall J. N., Januzzi B. T., Schneider D. P., Green R. F., 1995, ApJS, 99, 1
Liske J., Williger G. M., 2001, MNRAS, 328, 653
Lu L., Wolfe A. M., Turnshek D. A., 1991, ApJ, 367, 19
Meiksin A., 2007, Rev. Mod. Phys., submitted (arXiv:0711.3358)
Meiksin A., White M., 2004, MNRAS, 350, 1107
Madau P., Haardt F., Rees M. J., 1999, ApJ, 514, 648

Marziani P., Sulentic J. W., Dultzin-Hacyan D., Calvani M., Moles M., 1996, ApJS, 104, 37
McDonald P., Miralda-Escudé J., Rauch M., Sargent W. L. W., Barlow T. A., Cen R., 2001, ApJ, 562, 52
McIntosh D. H., Rix H.-W., Rieke M. J., Foltz C. B., 1991, ApJ, 517, L73
McLean B. J., Greene G. R., Lattanzi M. G., Pirenne B., 2000, in Manset N., Veillet C., Crabtree D., eds, ASP Conf. Ser. Vol. 216, Astronomical Data Analysis and Software Systems IX. Astron. Soc. Pac., San Francisco, p. 145
Murdoch H. S., Hunstead R. W., Pettini M., Blades J. C., 1986, ApJ, 309, 19
Natali F., Giallongo E., Cristiani S., La Franca F., 1998, AJ, 115, 397
Nusser A., Haehnelt M., 2000, MNRAS, 313, 364
Osterbrock D. E., 1989, Astrophysics of Gaseous Nebulae and Active Galactic Nuclei. University Science Book, Mill Valley, CA
Rauch M., Sargent W. L. W., Womble D. S., Barlow T. A., 1996, ApJ, 467, L5
Ricotti M., Gnedin N. Y., Shull J. M., 2000, ApJ, 534, 41
Rollinde E., Srianand R., Theuns T., Petitjean P., Chand H., 2005, MNRAS, 361, 1015
Saitta F., D'Odorico V., Bruscoli M., Cristiani S., Monaco P., Viel M., 2008, MNRAS, 385, 519 (Paper I)
Schaye J., 2001, ApJ, 559, 507
Schaye J., Theuns T., Rauch M., Efstathiou G., Sargent W. L. W., 2000, MNRAS, 318, 817
Scott J., Bechtold J., Dobrzycki A., Kulkarni P., 2000, ApJS, 130, 67
Springel V., 2005, MNRAS, 364, 1105
Springel V., White S. D. M., Jenkins A., Frenk C. S., Yoshida N. et al., 2005, Nat, 435, 629
Srianand R., Khare P., 1996, MNRAS, 280, 767
Sulentic J. W., Stirpe G. M., Marziani P., Zamanov R., Calvani M., Braito V., 2004, A&A, 423, 121
Telfer R. C., Zheng W., Kriss G. A., Davidsen A. F., 2002, ApJ, 565, 773
Tytler D., 1987, ApJ, 321, 69
Tytler D., Fan X.-M., 1992, ApJS, 79, 1
Tytler D. et al., 2004, ApJ, 617, 1
Vanden Berk D. E. et al., 2001, AJ, 122, 549
Vernet J., Dekker H., D'Odorico S., Pallavicini R., Rasmussen P. K., Kaper L., Hammer F., Groot P., the X-Shooter Team, 2008, Messenger, 130, 5
Viel M., Haehnelt M. G., Springel V., 2004, MNRAS, 354, 684
Viel M., Haehnelt M. G., Lewis A., 2006, MNRAS, 370, L51
Vrtilek J. M., Carleton N. P., 1985, ApJ, 294, 106
Williger G. M., Baldwin J. A., Carswell R. F., Cooke A. J., Hazard C., Irwin M. J., McMahon R. G., Storrie-Lombardi L. J., 1994, ApJ, 428, 574
Wilkes B. J., 1986, MNRAS, 218, 331
Zaroubi S., Viel M., Nusser A., Haehnelt M., Kim T.-S., 2006, MNRAS, 369, 734

This paper has been typeset from a TEX/LATEX file prepared by the author.